AN ALGORITHM FOR ROTATING AXISYMMETRIC FLOWS: MODEL, VALIDATION AND INDUSTRIAL APPLICATIONS

Gastón M. Mazzaferro, Sergio P. Ferro, Marcela B. Goldschmit

Center for Industrial Research, FUDETEC. Dr. Simini 250, B2804MHA Campana, ARGENTINA.

Key words. Axisymmetric flows, turbulent flows, k-ε model, finite element method.

Abstract. *The study of axisymmetric flows is of interest not only from an academic point of view, due to the existence of exact solutions of Navier Stokes equations, but also from an industrial point of view, since these kind of flows are frequently found in several applications.*

In the present work the development and implementation of a finite element algorithm to solve Navier Stokes equations with axisymmetric geometry and boundary conditions is presented. Such algorithm allows the simulation of flows with tangential velocity, including free surface flows, for both laminar and turbulent conditions. Pseudoconcentration technique is used to model the free surface (or the interface between two fluids) and the k-ε model is employed to take into account turbulent effects.

The finite element model is validated by comparisons with analytical solutions of Navier – Stokes equations and experimental measurements. Two different industrial applications are presented.

1. INTRODUCTION

In several fields of industry, there are processes that involve confined turbulent flows. The study of these flows often leads to an improvement in the performance of the processes, being numerical methods an optimal tool –sometimes the only viable– to carry out this kind of analysis. Examples of applications of numerical methods on industrial flow problems can be found in [1-3].

In steel industry, turbulent flows play an important role during the continuous casting process. These flows are essentially three-dimensional and the numerical solution must be found in a spatial domain with volumetric discretization. As a consequence, a huge number of nodes is required and the solutions become computationally expensive. However, there are processes that, in spite of their three-dimensional nature, may be assumed to be axisymmetric. In axisymmetric problems both the geometry and the driving forces do not depend on rotations around a symmetry axis and the flow only needs to be determined on any azimuthal plane. This represents an important reduction in the amount of degrees of freedom of the problem and in the computational cost of the numerical solution.

Several publications may be found in open literature reporting numerical results of rotating axisymmetric flow problems [4-9]. Most of these papers, consider swirl flows in sudden expansions with practical application in industrial combustors.

In this paper, we present a finite element algorithm to solve axisymmetric turbulent Navier Stokes equations with rotation and show its application to two steel industry problems: electromagnetic stirring of steel in round billet continuous casting and water flow inside a steel tube in a quenching pool.

The algorithm is described in the following section and its validation is presented in Section 3. The industrial applications of the algorithm are presented in Section 4. The last section is devoted to conclusions.

2. AXISYMMETRIC TURBULENT FLOW WITH SWIRLING

In this section we present the axisymmetric model for turbulent rotating flow. Turbulent effects are taken into account by means of the k-ε model together with wall function methods [10].

The mathematical model is formed by mass conservation equation (1), radial, azimuthal and axial components of Navier Stokes equations (2-4), turbulent kinetic

energy transport equation (5) and turbulent kinetic energy dissipation rate transport equation (6).

$$\frac{1}{r}\frac{\partial}{\partial r}\left(rv_r\right)+\frac{\partial v_z}{\partial z}=0 \tag{1}$$

$$\begin{aligned}&\rho\frac{\partial v_r}{\partial t}+\rho\left(v_r\frac{\partial v_r}{\partial r}-\frac{v_\theta^{\,2}}{r}+v_z\frac{\partial v_r}{\partial z}\right)=\\&\frac{1}{r}\left[\frac{\partial}{\partial r}\left(2r\mu^{ef}\frac{\partial v_r}{\partial r}\right)-2\mu^{ef}\frac{v_r}{r}+r\frac{\partial}{\partial z}\left(\mu^{ef}\left(\frac{\partial v_r}{\partial z}+\frac{\partial v_z}{\partial r}\right)\right)\right]-\frac{\partial P}{\partial r}+f_{b_r}\end{aligned} \tag{2}$$

$$\begin{aligned}&\rho\frac{\partial v_\theta}{\partial t}+\rho\left(v_r\frac{\partial v_\theta}{\partial r}+\frac{v_r v_\theta}{r}+v_z\frac{\partial v_\theta}{\partial z}\right)=\\&\frac{1}{r}\left[\frac{\partial}{\partial r}\left(r\mu^{ef}\left(\frac{\partial v_\theta}{\partial r}-\frac{v_\theta}{r}\right)\right)+\mu^{ef}\left(\frac{\partial v_\theta}{\partial r}-\frac{v_\theta}{r}\right)+\frac{\partial}{\partial z}\left(r\mu^{ef}\frac{\partial v_\theta}{\partial z}\right)\right]+f_{b_\theta}\end{aligned} \tag{3}$$

$$\begin{aligned}&\rho\frac{\partial v_z}{\partial t}+\rho\left(v_r\frac{\partial v_z}{\partial r}+v_z\frac{\partial v_z}{\partial z}\right)=\\&\frac{1}{r}\left[\frac{\partial}{\partial r}\left(r\mu^{ef}\left(\frac{\partial v_r}{\partial z}+\frac{\partial v_z}{\partial r}\right)\right)+\frac{\partial}{\partial z}\left(2r\mu^{ef}\frac{\partial v_z}{\partial z}\right)\right]-\frac{\partial P}{\partial z}+f_{b_z}+\rho\,gz\end{aligned} \tag{4}$$

$$\rho\frac{\partial k}{\partial t}+\rho\left(v_r\frac{\partial k}{\partial r}+v_z\frac{\partial k}{\partial z}\right)=\frac{\mu^{ef}}{r\sigma_k}\frac{\partial k}{\partial r}+\frac{\partial}{\partial r}\left(\frac{\mu^{ef}}{\sigma_k}\frac{\partial k}{\partial r}\right)+\frac{\partial}{\partial z}\left(\frac{\mu^{ef}}{\sigma_k}\frac{\partial k}{\partial z}\right)$$
$$+2\mu^t\left[\left(\frac{\partial v_r}{\partial r}\right)^2+\left(\frac{v_r}{r}\right)^2+\left(\frac{\partial v_z}{\partial z}\right)^2+\left(\frac{\partial v_r}{\partial z}\frac{\partial v_z}{\partial r}\right)-\left(\frac{\partial v_\theta}{\partial r}\frac{v_\theta}{r}\right)\right] \tag{5}$$
$$+\mu^t\left[\left(\frac{\partial v_r}{\partial z}\right)^2+\left(\frac{\partial v_\theta}{\partial r}\right)^2+\left(\frac{\partial v_\theta}{\partial z}\right)^2+\left(\frac{\partial v_z}{\partial r}\right)^2+\left(\frac{v_\theta}{r}\right)^2\right]-\rho\frac{C_\mu k^2}{\mu^t/\rho}$$

$$\rho\frac{\partial \varepsilon}{\partial t}+\rho\left(v_r\frac{\partial \varepsilon}{\partial r}+v_z\frac{\partial \varepsilon}{\partial z}\right)=\frac{\mu^{ef}}{r\sigma_\varepsilon}\frac{\partial \varepsilon}{\partial r}+\frac{\partial}{\partial r}\left(\frac{\mu^{ef}}{\sigma_\varepsilon}\frac{\partial \varepsilon}{\partial r}\right)+\frac{\partial}{\partial z}\left(\frac{\mu^{ef}}{\sigma_\varepsilon}\frac{\partial \varepsilon}{\partial z}\right)$$
$$+2\rho C_\mu C_1 k\left[\left(\frac{\partial v_r}{\partial r}\right)^2+\left(\frac{v_r}{r}\right)^2+\left(\frac{\partial v_z}{\partial z}\right)^2+\left(\frac{\partial v_r}{\partial z}\frac{\partial v_z}{\partial r}\right)-\left(\frac{\partial v_\theta}{\partial r}\frac{v_\theta}{r}\right)\right] \tag{6}$$
$$+\rho C_\mu C_1 k\left[\left(\frac{\partial v_r}{\partial z}\right)^2+\left(\frac{\partial v_\theta}{\partial r}\right)^2+\left(\frac{\partial v_\theta}{\partial z}\right)^2+\left(\frac{\partial v_z}{\partial r}\right)^2+\left(\frac{v_\theta}{r}\right)^2\right]-\rho\frac{C_2\varepsilon^2}{k}$$

In the above expressions, v_r, v_z, v_θ represent the three components of the averaged velocity, P is the averaged pressure, k the turbulent kinetic energy and ε its dissipation rate. The fluid is characterized by its density ρ and its viscosity μ. The effective viscosity μ^{ef} due to turbulent effects is given by $\mu^{ef}=\mu+\mu^t$, with

$$\mu^t=C_\mu\rho\sqrt{k}\,L \tag{7}$$

where L is the turbulence characteristic length

$$L=k^{3/2}/\varepsilon \tag{8}$$

External volumetric forces acting on the fluid are represented by f_b excepting the gravitational term, which is explicitly written. Finally C_1, C_2, C_μ, σ_k and σ_ε are the constants of the k-ε model that were calibrated by Launder and Spalding [10].

2.1 Algorithm

In order to solve the highly nonlinear system (1-8) a *k-L* predictor ε-corrector algorithm [11-13] is used for each time step. The algorithm is presented in Figures 1 and 2. There is a main iteration loop that checks the convergence of the mixing length. Within this loop there are two phases: the predictor phase where the three components of the velocity and the turbulent kinetic energy (k) are calculated and the corrector phase where the dissipation rate of k is calculated (ε).

This algorithm has been previously used to solve different types of three-dimensional industrial flows [14-17]. The contribution of this paper to the general formulation of the algorithm is a modification introduced on the predictor phase; the azimuthal component of the velocity is calculated as a separated variable after solving Navier Stokes equations for the axial and radial components of the velocity. By uncoupling the azimuthal component of the velocity, the problem keeps the numeric complexity of a non-rotating flow problem.

When dealing with flows with free surface or flows with an interface between fluids, the pseudoconcentration technique [18] was employed. This is an eulerian method (the mesh remains fixed in contraposition to lagrangian method where the mesh is updated following the surface movement) and is generally preferred for industrial applications due to its simplicity [19-20]. A scalar field C –pseudoconcentration– is introduced, which satisfies a convection equation.

$$\frac{\partial C}{\partial t} + \left(v_r \frac{\partial C}{\partial r} + v_z \frac{\partial C}{\partial z} \right) = 0 \tag{9}$$

In problems involving pseudoconcentration, a transient algorithm is always used even when only the steady state solution is of interest. Equation (9) is solved once the flow problem (Equations 1-8) has converged for the given time step. A critical value C_c determines the position of the interface (or free surface). Physical properties of first fluid are used wherever $C > C_c$. Reciprocally, physical properties of second fluid are used wherever $C < C_c$.

For each time step, the position of the surface $C = C_c$ is updated with Equation (9). However, during the evolution of the surface strong gradients of C may be generated, which could lead to numerical instabilities. In order to avoid the formation of such gradients, the pseudoconcentration C on each point is redefined according to its distance, d, to the free surface [20] $C = C_c + d\ \sigma \operatorname{sgn}(C - C_c)$ (where σ is a constant). This expression makes the pseudoconcentration distribution smooth along the domain without modifying the position of the free surface.

2.2 Boundary Conditions

In order to solve the system of equations (1-9), proper boundary conditions must be applied on domain limits.

On solid walls boundaries, wall function method [10] was used. In this method a boundary layer of thickness Δ is assumed to lay between the wall and the numerical domain. Normal component of the velocity v_n, shear stresses τ^w and turbulent variables on domain boundary are set according to

$$v_n = 0 \quad \tau^w = \rho v_f^{\,2} \quad k^w = \frac{v_f^{\,2}}{\sqrt{C_\mu}} \quad \varepsilon^w = \frac{v_f^{\,3}}{\kappa \Delta}, \tag{10}$$

where κ=*0.4* is the Von Karman constant and v_f, the friction velocity, is related to the tangential velocity v_t and wall rugosity E by $v_t \kappa = v_f \ln\left(\rho E v_f \Delta / \mu\right)$.

On symmetry axis, all variables were assumed to have no radial derivative with the velocity having only axial component.

The rest of the boundaries are determined by the limits of the numerical domain. On these boundaries, either Dirichlet boundary conditions or homogeneous Neumann boundary conditions were applied to all variables. In the first case the following relations were used to impose the turbulent variables in term of the boundary value of the velocity $\underline{v}^i$,

$$k^i = \alpha \, |\underline{v}^i|^2 \qquad \varepsilon^i = k^{i\,3/2} / L \tag{11}$$

where α is a constant determined from experiments and L is the characteristic length scale of the problem.

For equation (9) the value of C is imposed only on those boundaries where the fluid is entering the domain.

2.3 Finite element implementation

The finite element implementation of this algorithm is obtained by discretizing the system of equations (1-6) and –eventually– the pseudoconcentration equation (9) by weighted residual method using linear isoparametric elements.

The Streamline Upwind Petrov Galerkin method developed by Hughes and Brooks [21] was employed. The corresponding weighting functions, in terms of the shape function h^I and nodal values $\underline{\hat{u}}^I$, have the following expressions

$$w_r = \left[h^I + \tau \left(v_r \frac{\partial h^I}{\partial r} + v_z \frac{\partial h^I}{\partial z} \right) \right] \hat{u}_r^I$$

$$w_z = \left[h^I + \tau \left(v_r \frac{\partial h^I}{\partial r} + v_z \frac{\partial h^I}{\partial z} \right) \right] \hat{u}_z^I \tag{12}$$

$$w_\theta = \left[h^I + \tau \left(v_r \frac{\partial h^I}{\partial r} + v_z \frac{\partial h^I}{\partial z} \right) \right] \hat{u}_\theta^I$$

where the intrinsic time τ depends on the center element velocity $\underline{v^c}$ and the element characteristic lengths l_r and l_z,

$$\tau = \frac{1}{2} \frac{1}{v_r^{c2} + v_z^{c2}} \sum_{i=r,z} \beta_i v_i^c l_i \tag{13}$$

The parameter $\beta_i = \coth Pe_i - Pe_i^{-1}$ is function of the Péclet number of the element, Pe_i, defined by $Pe_i = l_i \left| v_i^c \right| \rho / 2\mu^{ef}$.

It can be observed that due to the two-dimensional nature of the numerical domain, the azimuthal velocity was not considered in the weighting functions. Consistently, it was neither used in the expression for the intrinsic time τ. A detailed description of the formulation and the complete expression of the resulting finite element equations can be found in [22].

The trapezoidal rule was used for time discretization. A Gauss-Seidel approach was adopted in the iteration scheme. For each equation both Picard and Newton Raphson linearization were implemented.

3. MODEL VALIDATION

In order to validate the method, different axisymmetric rotating flows were considered. The first two cases correspond to laminar flows where analytical solution

can be found. The third example corresponds to turbulent flow and numerical results are compared to experimental measurements obtained from the open literature.

3.1 Couette Flow

As a first example, Couette flow is analyzed. Couette flow is driven by two concentric cylinders in rotational motion. A scheme of the problem together with its boundary conditions is shown in Figure 3.

The resulting flow field is azimuthal depending only on the radial coordinate, the radii of the cylinders r_1, r_2 and their angular velocity Ω_1 and Ω_2.

$$v_\theta(r) = \frac{1}{r}\left(\frac{\Omega_1 - \Omega_2}{r_1^{-2} - r_2^{-2}}\right) + r\left(\frac{\Omega_1 r_1^2 - \Omega_2 r_2^2}{r_1^2 - r_2^2}\right) \tag{14}$$

Numerical results on a mesh with only ten radial elements are in agreement with the analytical result as can be seen on Figure 4.

3.2 Azimuthally Stirred Flow

In order to validate the model for flows with free surface driven by an external azimuthal force, the flow inside a cylindrical tank of radius R when a volumetric force $f_{b\theta} = (f_0 / R)\, r$ is applied on a fluid with viscosity μ, is simulated. The steady state solution for such a flow is a pure rotation with a cubic profile for the azimuthal velocity,

$$v_\theta = v_0\left(\chi - \chi^3\right) \tag{15}$$

where $\chi = r/R$ is the dimensionless radial position and $v_0 = \dfrac{R^2 f_0}{8\mu}$.

The free surface profile is given by the following expression,

$$h(r) = h_0\left[1 + \gamma\left(\frac{\chi^2}{2} - \frac{\chi^4}{2} + \frac{\chi^6}{6} - \frac{1}{8}\right)\right] \tag{16}$$

where h_0 is the initial height of fluid and $\gamma = v_0^2/gh_0$ is a dimensionless parameter which relates centrifugal force to gravitational force. Boundary conditions are shown in Figure 5.

Results for $R = 50\ mm$, $h_0 = 50\ mm$, $v_0 = 625\ mm/s$, $\gamma = 0.8$ are presented in Figures 6 and 7. Both the velocity and the free surface profile are plotted together with their error. The model was run on a 6500 elements mesh. 300 time steps were needed to reach steady state, starting from a flat surface initial condition.

3.3 Rotating flow in a pipe with sudden expansion

As a final validation of the method we present the simulation of a turbulent rotating flow inside a combustor. This example was taken from a work by S. Ahmed and A. Nejad [23] who presented experimental results of the problem.

The combustor has an inlet radius $R_i=50.8\ mm$ and the step has a height $H=25.4\ mm$. The authors measured the different components of the velocity along the radius at several stations located downstream the expansion for a distance $18\ H$.

The swirl number,

$$S = \int_0^{R_i} v_z\, v_\theta\, r^2 dr \Big/ R_i \int_0^{R_i} {v_z}^2\, r\, dr \qquad (17)$$

is introduced as a quantitative indicator of this rotational speed. The value $S=0.5$ was considered in our calculations in order to compare results with Ahmed and Nehad measurements.

The velocity measurements [23] were used as boundary conditions at the inlet and outlet of the combustor (${v_r}^i, {v_z}^i, {v_\theta}^i$ and ${v_r}^o, {v_z}^o, {v_\theta}^o$), as seen in Figure 8. Equations (11) were applied to impose boundary condition on turbulent variables (k^i, ε^i and k^o, ε^o), using $\alpha = 0.01$, and the combustor radii as characteristic lengths.

A 6500 elements mesh was used. A preliminary solution was obtained with a simple algebraic turbulence model whose results were used as initial guess for the final calculation. Convergence was achieved after 19 cycles of the main iteration loop.

The numerical results for axial and azimuthal components of the velocity are compared to measurements in Figure 9. A reasonable agreement between numerical and experimental data is observed. Discrepancies in the results are due to the isotropic turbulence hypothesis, implicitly assumed in the k-ε model. A non isotropic turbulence model, as those presented in reference [9], should be implemented in order to achieve a more accurate solution.

4. INDUSTRIAL APPLICATIONS

Several processes in the seamless steel tubes manufacture involve turbulent flows that may be regarded as axisymmetric. Such processes have strong influence on the final quality of the tubes and need to be fully understood in order to be optimized. Numerical modeling is an important tool to understand the mechanisms taking part in these processes.

4.1 Electromagnetic Stirring in round billets mould

In different stages of the continuous casting processes the liquid steel interacts with a buoyant layer of slag or casting powder. The stability of this interface influences the quality of the final product. Modifications of this interface due to variations in the liquid steel flow may produce slag entrapment inside the liquid steel, which generates non-metallic inclusions in the final product. Thus, the analysis of the behavior of the interface steel/slag under given operative conditions is of importance from an industrial point of view.

During solidification process in round billets moulds, the liquid steel is often electromagnetically stirred in order to produce a good chemical and thermal homogenization. This stirring process modifies the interface between the steel and casting powder layer in the top of the mould. The influence of the electromagnetic stirring (EMS) operative parameters (number of coils, current intensity and frequency on stirrer coils) on interface stability was analyzed by finite elements method.

The EMS effect is included in the model by the application of external azimuthal forces. The electromagnetic forces induced in the steel by the EMS were calculated by Maldovan et al [15], as function of EMS parameters.

A 395 mm diameter mould with 6 coils EMS operating at 3 Hz and different current intensities is analyzed. The force field is not strictly axisymmetric having some variations along the azimuthal coordinate, thus the distribution of forces was taken from an average azimuthal plane.

A uniform velocity profile (v_z^i, consistent with a 0.34 m/min casting speed), turbulent kinetic energy and its dissipation rate were imposed at the nozzle entrance as boundary conditions using equations (11), with α = 0.01 and $L = R$, the nozzle radius (see Figure 10). Wall functions were used to impose boundary conditions at the mould and nozzle and the pseudoconcentration method was used to track the liquid interface

between steel ($\rho = 7500$ Kg/m^3 , $\mu = 5.3\ 10^{-3}$ Kg/ms) and slag ($\rho = 2500$ Kg/m^3 , $\mu = 0.1$ Kg/ms).

The numerical domain consists of 22000 elements. Around 200 time steps were needed to achieve a steady state, starting from a flat surface initial condition.

Figures 11 and 12 show the axial and azimuthal velocity distribution in the mould for increasing current intensities. Figure 13 shows the interface profile for each case, indicating the height difference (ΔH) between the nozzle side and the mould side.

Main conclusions of the numerical analysis are:

- EMS diminishes the jet penetration length in the mould. The stronger the current intensity, the shorter the jet. Beyond a critical current intensity the jet is broken and a recirculation zone appears, with liquid steel going up through the center of the mould and going down along mould walls (see Figure 11). Similar results have already been reported by Kunstreich et al [24].

- EMS generates an important rotation in the liquid steel (Figure 12). High rotational velocities near the mould walls avoid the formation of solidification dendrites, increasing the thickness of the axial solidification layer.

- Turbulence is increased and better distributed inside the mould (particularly below the interface), improving chemical and thermal homogenization of the liquid steel. Component stratification decreases and the flow removes small bubbles that may have formed between dendrites. On the other hand, this increment of turbulence may produce more wear on nozzle walls and may increase the chances of casting powder entrapment.

- The interface suffers an inclination due to the effect of centrifugal forces (Figure 13).

4.2 Heat treatment of steel tubes in water quenching pools

Once the steel tubes are rolled, they are thermally treated in order to enhance their mechanical properties. The quenching process consists in heating the tube up to 800° C and cooling it rapidly by a sudden submersion in water. Inside the quenching pool several jets of water are directed towards the outer wall of the tube while an important amount of water is injected inside the tube by means of a coaxial nozzle. It is important to achieve a homogenous heat withdrawal from the tube in order to avoid inhomogeneous

mechanical properties. Consequently, the flow of water is expected not to suffer important modifications along the inner walls of the tube.

The influence of different parameter of the tube-nozzle system on the flow around the tube was analyzed. Figure 14 shows a scheme of the nozzle-tube system. Water was injected into the tube by a conical nozzle at a flow rate of 550 m^3 /h. The nozzle outlet diameter (D_{out}) and nozzle-tube distance (L_{bt}) were varied as indicated in Table I. In the last two cases rotational velocity was also imposed at nozzle entrance (radius R_{in} *=100 mm*).

	D_{out}	L_{bt}	S
Case I	85 mm	10 mm	0.0
Case II	85 mm	200 mm	0.0
Case III	120 mm	10 mm	0.0
Case IV	120 mm	200 mm	0.0
Case V	85 mm	10 mm	0.344
Case VI	85 mm	200 mm	0.344

Table 1. Heat treatment of steel tubes in water quenching pools. Values of model variables.

Dirichlet boundary conditions were imposed for all variables at the nozzle entrance ($v_r^{\,i}$, $v_z^{\,i}$, $v_\theta^{\,i}$, k^i, ε^i; with $\alpha = 0.01$ and $L = 100$), and wall functions were used at nozzle and tube walls (see Figure 15). A linear-constant profile was imposed for rotational velocity according to Figure 16.

Around 45000 elements were used in the mesh. A preliminary solution was obtained using a simple algebraic turbulence model which was then used as initial guess for the final calculation. Convergence was achieved after 16 iterations.

Flow rate inside the tube should be high enough to reach a significant cooling rate. Obviously, for a given nozzle flow rate, the smaller the nozzle diameter the higher the velocities. For cases I-II the high velocities of the jet introduce a large amount of water from the pool on the tube. There is a higher flow rate in the tube for cases I-II than for cases III-IV. As a consequence the water velocity in the inner wall of the tube is also higher in cases I-II than in cases III-IV. This may be observed in Figure 17 where the axial velocity distribution has been plotted for cases I-IV.

Figure 17 also shows that for nozzles with large diameter (cases III and IV) the axial velocity along the inner wall of the tube is more homogenous than for nozzles with a small diameter (cases I and II). In other words, the flow has a short entry length (the

distance along the tube for the flow to become fully developed) when the nozzle diameter is large.

Flow rate inside the tube is hardly affected by modifying the nozzle-tube distance. The main difference in flow pattern is the reduction of the entry length for large separation distance (cases II and IV), since the jet widens as it travels from the nozzle to the tube.

A detail of the flow near the edge of the tube is depicted in Figure 18. For each case, a recirculation zone may be observed at the tube inner wall. The recirculation zone can also be seen on Figure 19 where the axial velocity of the water on the inner wall of the tube is plotted as function of the distance along the tube. In all cases there is a recirculation zone ($v_z<0$) at the tube entrance, then the velocity increases up to a given value (which is around one half of the final value) and finally increases again to reach its final value. Both the recirculation zone and the intermediate "plateau" are undesired effects since they lead to inhomogeneous cooling.

In order to achieve a more uniform velocity distribution along the wall, the introduction of a rotational component in the flow injected by the nozzle is analyzed. Industrially, a rotational component in the flow could be induced by placing a deflector in the nozzle. The idea is to enhance the widening of the jet coming out of the nozzle. The addition of rotational velocity (cases V and VI) tends to modify the flow distribution at the tube entrance, shortening the entry length, as presented in Figure 20.

5. CONCLUSIONS

A finite element algorithm was implemented to solve Navier Stokes equation for axisymmetric rotating flows. The numerical model can represent turbulent flows and flows with free surface or an interface between two fluids.

A solving method is proposed in which the azimuthal component of the velocity is uncoupled from the Navier-Stokes equation, keeping the numeric complexity of two-dimensional problems. The SUPG technique was used in the discretization but the rotational velocity was not considered in the weighting functions.

Numerical results were validated by comparisons with analytical solutions and experimental measurements.

The model was used to analyze two different processes on steel industry: the liquid steel flow inside round billet mould and water flow inside a tube in a quenching pool

Flow inside the mold was studied with focus on the influence of the EMS on flow properties. It was found that the EMS does not only create a rotational movement in the mold but also diminishes the jet penetration and even generates recirculation flow with steel going up through the centerline of the mold. An increment in turbulence was also observed which is useful to improve transport phenomena but may increase wear of mold walls. Finally numerical calculations have shown a slight inclination of the interface steel/casting powder due to centrifugal forces.

In the quenching pool analysis, the influence of different parameters on the flow inside the tube was studied. It was found that an increment on nozzle diameter or nozzle-tube distance, reduce the entry length in the tube and improve the homogeneity of the velocity on the inner tube wall. Also the introduction of a rotational component of the velocity in the jet will contribute in reducing the entry length.

NOMECLATURE

C	pseudoconcentration function
C_1	constant for k-ε model
C_2	constant for k-ε model
C_c	critical value of pseudoconcentration
C_μ	constant for k-ε model
D_{out}	outlet diameter for quenching pool nozzle
E	friction factor
H	combustor step height
L	mixing length
L_{bt}	nozzle – tube distance
P	pressure
Pe	elemental Peclet number
R	tank radius/mold nozzle radius/combustor inlet radius
R_{in}	inlet radius for quenching pool nozzle
S	swirl number
U_{cl}	combustor centerline velocity
d	distance to the free surface or interface
f_0	constant for applied force on stirred flow problem
f_b	volumetric force
g	gravitational acceleration
h^I	shape function
$h(r)$	free surface profile in stirred flow problem
h_0	initial height of fluid in stirred flow problem
k	turbulent kinetic energy
l	characteristic length of the element
r	radial coordinate
r_1, r_2	cylinder radii in Couette flow
t	time
$\hat{u}^I$	nodal velocity
v_0	characteristic velocity for stirred flow problem
v^c	center element velocity
v_f	friction velocity
v_n	normal component of the velocity
v	velocity
v_t	tangential component of the velocity
w	weighting function
z	axial coordinate

Greek symbols

Δ width of boundary layer
ΔH height difference between the nozzle side and the mould side
Ω_1, Ω_2 cylinders angular velocities in Couette flow
α constant for boundary condition on k
β SUPG parameter
γ parameter for stirred flow problem
ε turbulent kinetic energy dissipation rate
χ dimensionless radial coordinate
κ Von Karman constant
μ^t turbulent viscosity
μ^{ef} effective viscosity
ρ density
τ characteristic time for SUPG formulation
τ_w wall shear stresses
σ constant for pseudoconcentration redefinition
σ_k constant for k-ε model
σ_ε constant for k-ε model

Subscripts
r radial component
z axial component
θ azimuthal component

Superscripts
i boundary condition at the inlet
o boundary condition at the outlet
w boundary condition on solid walls

ACKNOWLEDGEMENTS

This research was financed by companies of the TENARIS group.

REFERENCES

[1] Mazumdar D., Guthrie R.I.L. On the numerical calculation and non-dimensional representation of velocity fields in bubble-stirred ladle systems. *Steel Research* 1993; **64**: N° 6; 286-291.

[2] Joo S., Guthrie R.I.L. Inclusion behavior and heat-transfer phenomena in the steelmaking tundish operations: Part I. Aqueous modeling. *Metallurgical Transactions B* 1993; **24**: 755-765.

[3] Najjar F.M., Thomas B.G., Hershey D.E. Numerical study of steady turbulent flow trough bifurcated nozzles in continuous casting. *Metallurgical and Material Transactions B* 1995; **26B**: 749-765.

[4] Iacovides H., Theofanopoulos I.P. Turbulence modeling of axisymmetric flow inside rotating cavities. *International Journal of Heat and Fluid Flow* 1991; **12**: N° 1; 2-11.

[5] Guo B., Langrish T.A.G., Fletcher D.F. Simulation of turbulent swirl flow in axisymmetric sudden expansion. *AIAA Journal* 2001; **39**: N° 1; 96-102.

[6] Pisi Lu, Semião V. A new second-moment closure approach for turbulent swirling confined flows. *International Journal for Numerical Methods in Fluids* 2003; **41**: 133-150.

[7] Yang X and Ma H, Computation of strongly swirling confined flows with cubic eddy viscosity turbulence models. *International Journal for Numerical Methods in Fluids* 2003; **43**: 1355-1370

[8] Yang X and Ma H, Linear and nonlinear eddy viscosity turbulence model for a confined swirling coaxial jet. *Numerical Heat Transfer B* 2003*;* **43**: 289-305

[9] Sharif, M. A. R. and Wong Y.K.E., Evaluation of the performance of three turbulence closure models in the prediction of confined swirling flows. *Computer and Fluids*, 1995; **24,** 81-100**.**

[10] Launder B., Spalding D. The numerical computation of turbulent flows. *Computer Methods in Applied Mechanics and Engineering* 1974; **3**: 269-289.

[11] Goldschmit M.B. Modelado de flujo turbulento. Aplicaciones a la colada continua de aceros. *Tesis Doctoral*, Universidad Nacional del Litoral, Santa Fe, Argentina, 1996.

[12] Goldschmit M.B. and Cavaliere M.A., "Modelling of turbulent recirculating flows via an iterative (k-L)-predictor / (ε)-corrector scheme", Applied Mechanics Review, 48, 11, 1995.

[13] Goldschmit M.B. and Cavaliere M.A., "An iterative (k-L)-predictor / (ε)-corrector algorithm for solving (k-ε) turbulent models", Engineering Computations, 14, 4, 441-455, 1997.

[14] Príncipe R.J., Goldschmit M.B. Las condiciones de contorno sobre la pared en el modelado de flujo turbulento. *Proc. VI Congreso Argentino de Mecánica Computacional, MECOM'99*, Mendoza, Argentina, 1999.

[15] Maldovan M., Príncipe J., Sánchez G., Pignotti A., Goldschmit M. Numerical modeling of continuous casting of rounds with electromagnetic stirring. *European Congress on Computational Methods in Applied Sciences and Engineering, ECCOMAS 2000*, Barcelona, Spain, 2000.

[16] Goldschmit M.B., Ferro S.P., Príncipe R.J., Coppola Owen H. Numerical modeling of liquid steel flow in continuous casting processes. *VII International Seminar on Recent Advances in Fluid Mechanics, Physics of Fluids and Associated Complex Systems*, Buenos Aires, Argentina, 2001.

[17] Goldschmit M.B., Coppola Owen H. Numerical modeling of gas stirred ladles. *Ironmaking and Steelmaking* 2001; **28**: 337-341.

[18] Thompson E. Use of the pseudo-concentration to follow creeping viscous flows during transient analysis. *International Journal for Numerical Methods in Engineering* 1986; **6**: 749-761.

[19] Ilinca F., Hétu J. Finite element solution of three-dimensional turbulent flows applied to mold-filling problems. *International Journal for Numerical Methods in Fluids* 2000; **34**: 729-750.

[20] M. B. Goldschmit, S. P. Ferro and A. H. Coppola Owen. "Modeling of liquid steel flow with free surface". Progress in Computational Fluid Dynamics, **4**, 1, 12-19, 2004

[21] Hughes T.J.R., Brooks A.N. A theoretical framework for Petrov-Galerkin methods with discontinuous weighting functions: Application to the streamline-upwind procedure. *Finite Element Fluids*, John Wiley & Sons (eds); 1982, Chapter 3; pp. 47-65.

[22] Mazzaferro G.M. Modelado de flujos de acero líquido con interfases. Desarrollo de un modelo de elementos finitos axilsimétrico de flujo turbulento. *Tesis de Ingeniería Mecánica*, Facultad de Ingeniería, Universidad de Buenos Aires, Buenos Aires, Argentina, 2003.

[23] Ahmed S., Nejad A. Velocity measurements in a research combustor, Part. I: Isothermal Swirling Flow. *Experimental Thermal and Fluid Science* 1992; **5**: 162-174.

[24] Kunstreich S., M.C. Nové, D. Yves. Recent Results in Double Coil Electromagnetic Stirring. *Developments in Continuous Casting of Blooms and Billets for Improved Quality and Productivity*, The Royal Society, London, UK, 1998.

Begin Program

- *Initialize variables*
- *Compute Mixing length and Turbulent viscosity*
- *Initialize time t=0*
- *Begin temporal loop*
  - *Update time t=t+dt*
  - *Initialize iteration index i=0*
  - *Begin main iteration loop*
    - *Set i=i+1*
    - *Predictor Phase: compute velocity, k*
    - *Corrector Phase: compute ε*
    - *Check convergence of Mixing Length*
  - *End main iteration loop*
  - *Solve pseudoconcentration equation if necessary (Eq. 9')*
  - *Check if steady state has been reached*
- *End temporal loop*

End program

Figure 1. General Algorithm.

Begin Predictor phase

- *Solve radial and axial Navier Stokes equations (Eq. 2 and 4)*
- ***Solve azimuthal Navier Stokes equation*** *(Eq. 3)*
- *Compute friction velocity using wall functions method* ***(Eq.10)***
- *Compute wall tensions and boundary values for k and* ε
- *Update turbulent viscosity (Eq. 7)*
- *Solve transport equation for k (Eq. 5)*
- *Update turbulent viscosity (Eq. 7)*
- *Check convergence in velocity and k.*

End predictor phase

Begin corrector phase

- *Solve transport equation for* ε *(Eq. 6)*
- *Check convergence in* ε
- *Update turbulent viscosity (Eq. 7)*
- *Update Mixing length (Eq. 8)*

End corrector phase

Figure 2. Predictor and corrector phases of the algorithm.

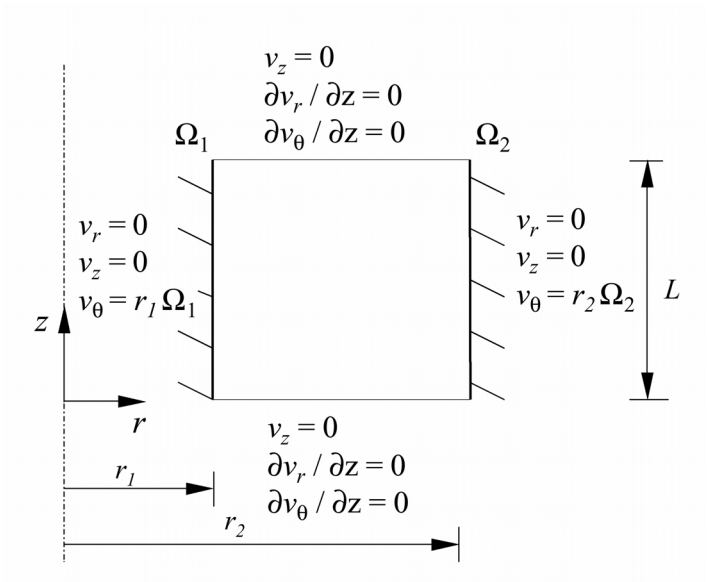

Figure 3. Boundary conditions for Couette flow.

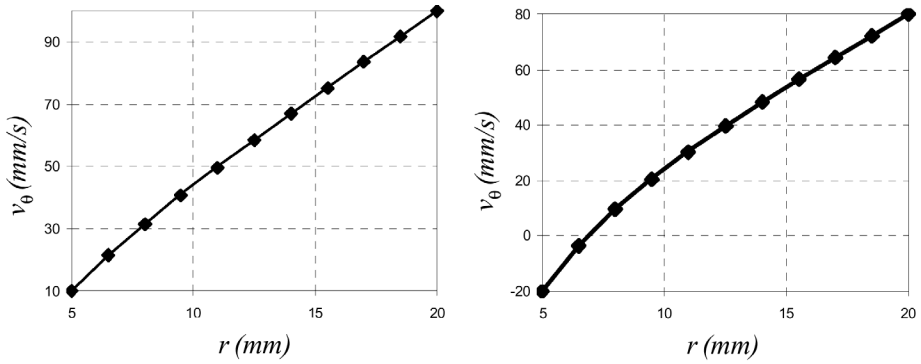

a) $\Omega_1 = 2/s$; $\Omega_2 = 5/s$ *b)* $\Omega_1 = -4/s$; $\Omega_2 = 4/s$

Figure 4. Comparison of analytical expression (lines) and numerical results (dots) for Couette flow.

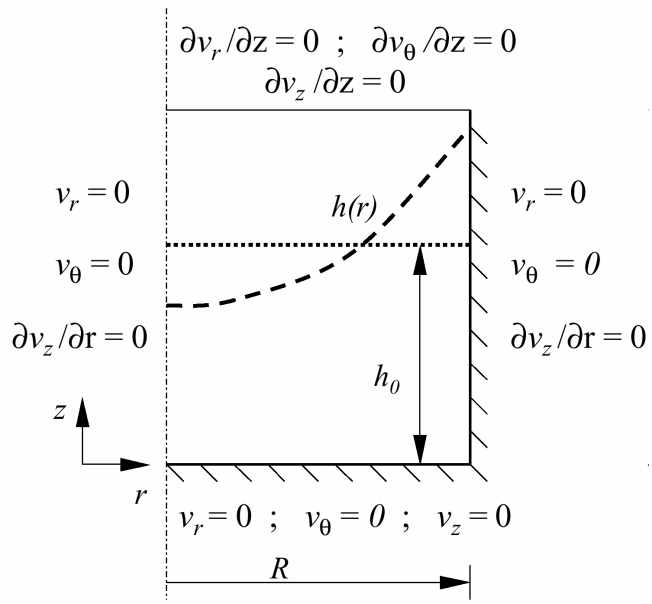

Figure 5. Boundary conditions for azimuthally stirred flow.

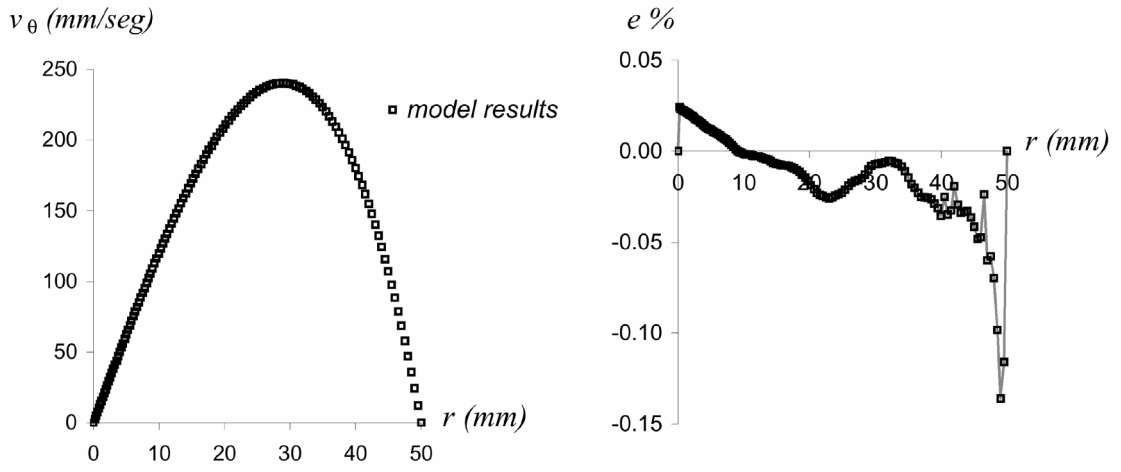

Figure 6. Numerical results for azimuthally stirred flow, and its error.

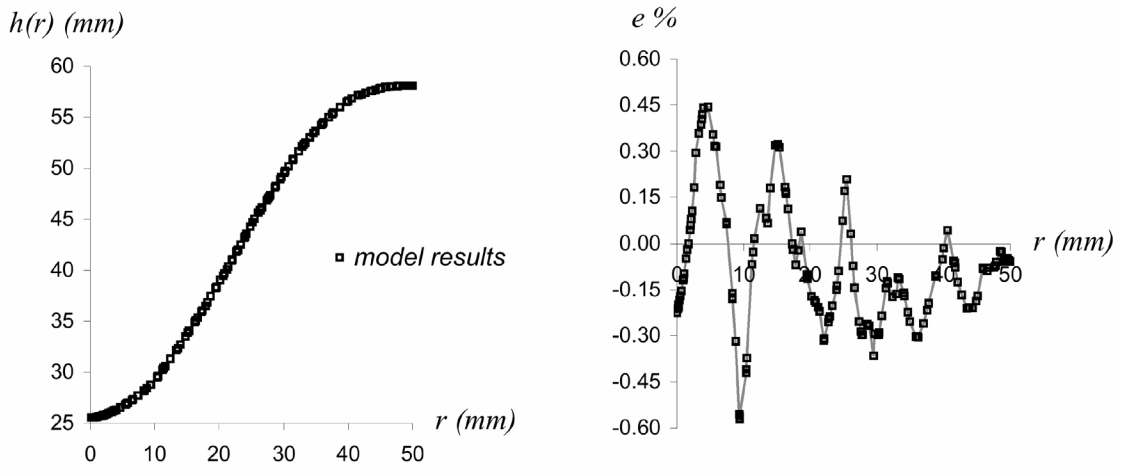

Figure 7. Numerical results for free surface profile, and its error.

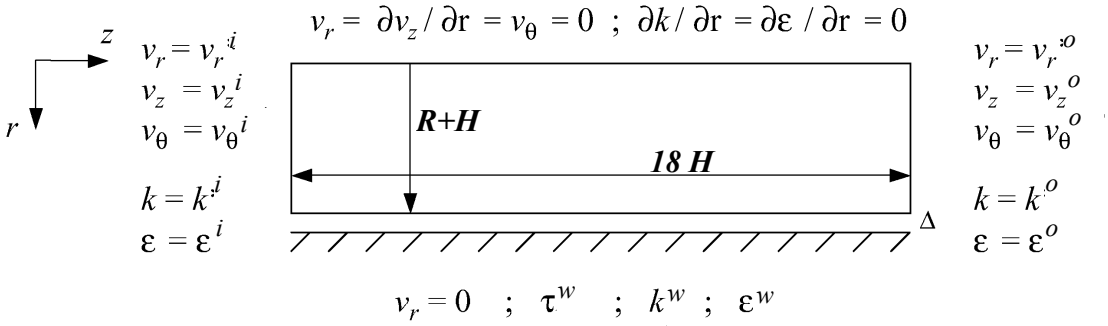

Figure 8. Boundary conditions for Rotating flow in a pipe with sudden expansion. Dirichlet boundary conditions at the inlet and outlet were taken from measurements [23].

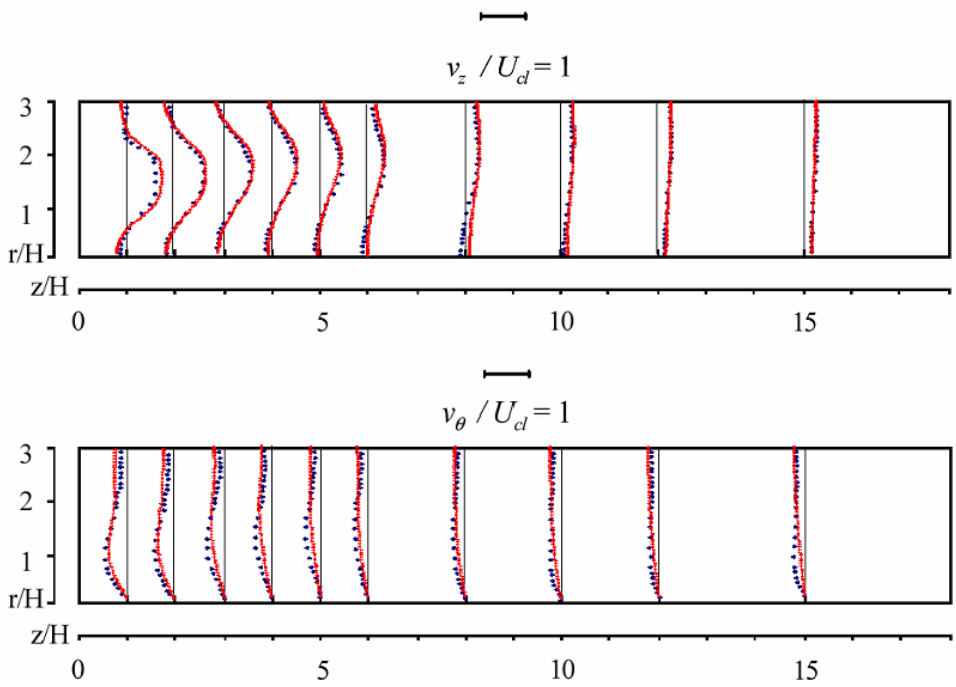

Figure 9. Flow field in a combustor. Numerical results (lines) and experimental measurements (dots). Velocities are expressed in terms of the centerline velocity U_{cl}

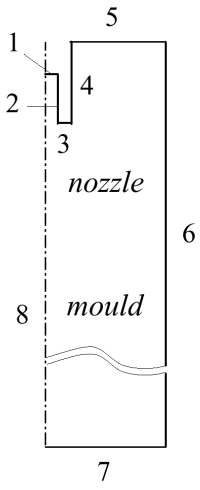

Boundary Conditions:

1. Nozzle entrance: $v_r = v_\theta = 0$; $v_z = 395$ *mm/s;* $k = k^i$; $\varepsilon = \varepsilon^i$; $C^i = 1$.

2. Inner nozzle wall: $v_r = 0$; τ^w ; k^w ; ε^w .

3. Nozzle edge: $v_z = 0$; τ^w ; k^w ; ε^w .

4. Outer nozzle wall: $v_r = 0$; τ^w ; k^w ; ε^w .

5. Domain limit: $\partial v_r / \partial z = \partial v_z / \partial z = \partial v_\theta / \partial z = 0$; $\partial k / \partial z = \partial \varepsilon / \partial z = 0$; $C = 0$.

6. Mould wall: $v_r = 0$; τ^w ; k^w ; ε^w .

7. Domain limit: $\partial v_r / \partial z = \partial v_z / \partial z = \partial v_\theta / \partial z = 0$; $\partial k / \partial z = \partial \varepsilon / \partial z = 0$.

8. Symmetry axis: $v_r = v_\theta = 0$; $\partial v_z / \partial r = 0$; $\partial k / \partial r = \partial \varepsilon / \partial r = 0$.

Figure 10. Boundary conditions for Electromagnetic Stirring in round billets mould. Turbulent variables at inlet were imposed using Eq. 11 with α=0.01 and the nozzles radius as characteristic length.

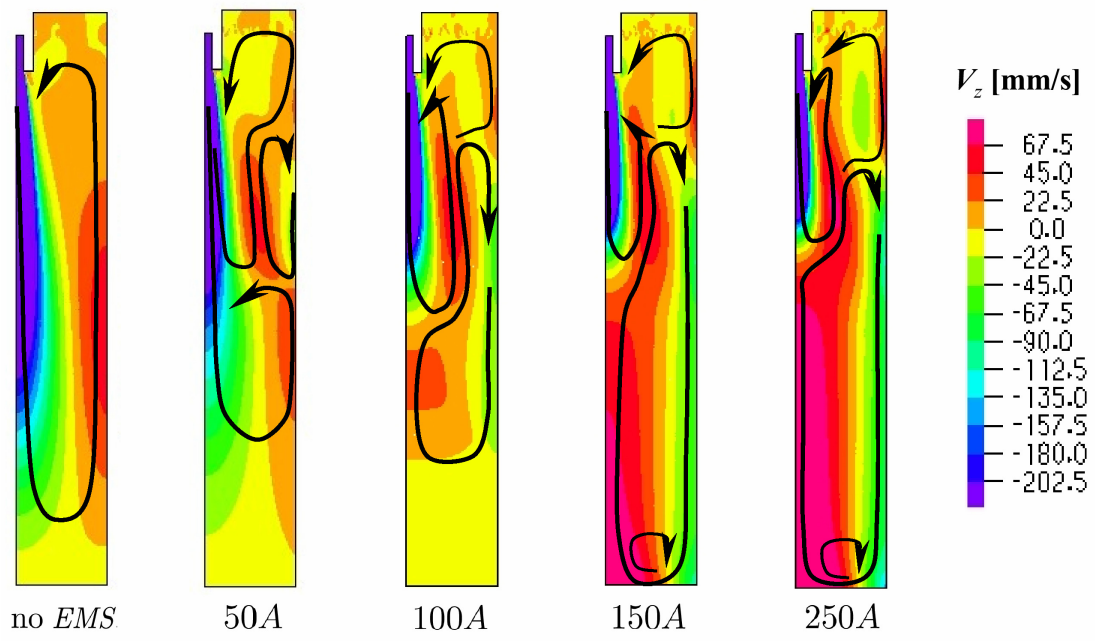

Figure 11. Electromagnetic Stirring in round billets mold. Axial velocity field and recirculation zones.

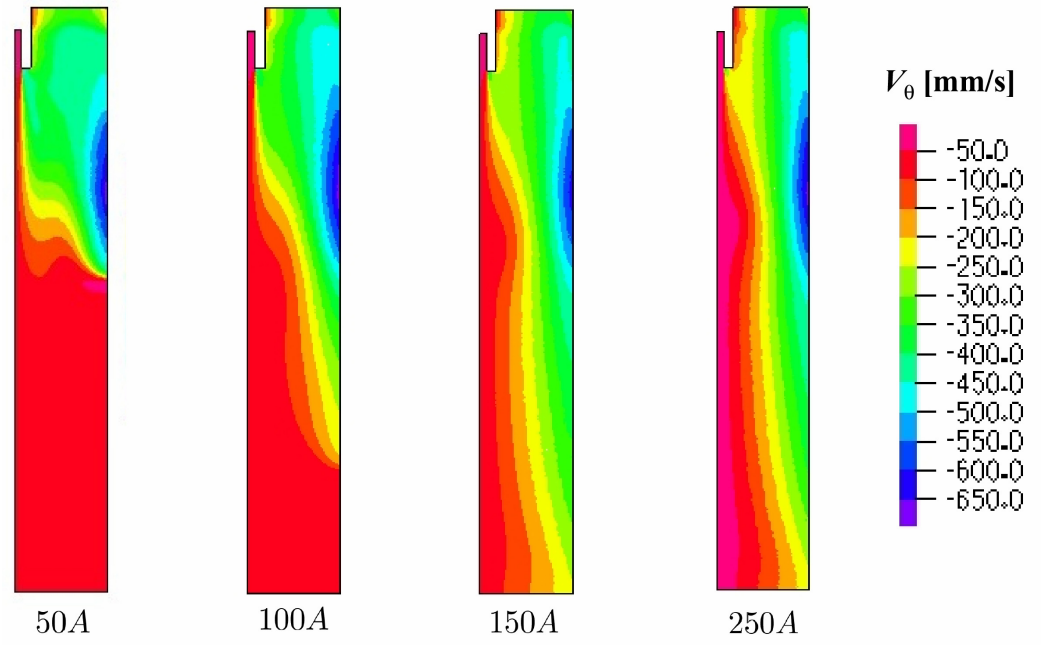

Figure 12. Electromagnetic Stirring in round billets mold. Azimuthal velocity field.

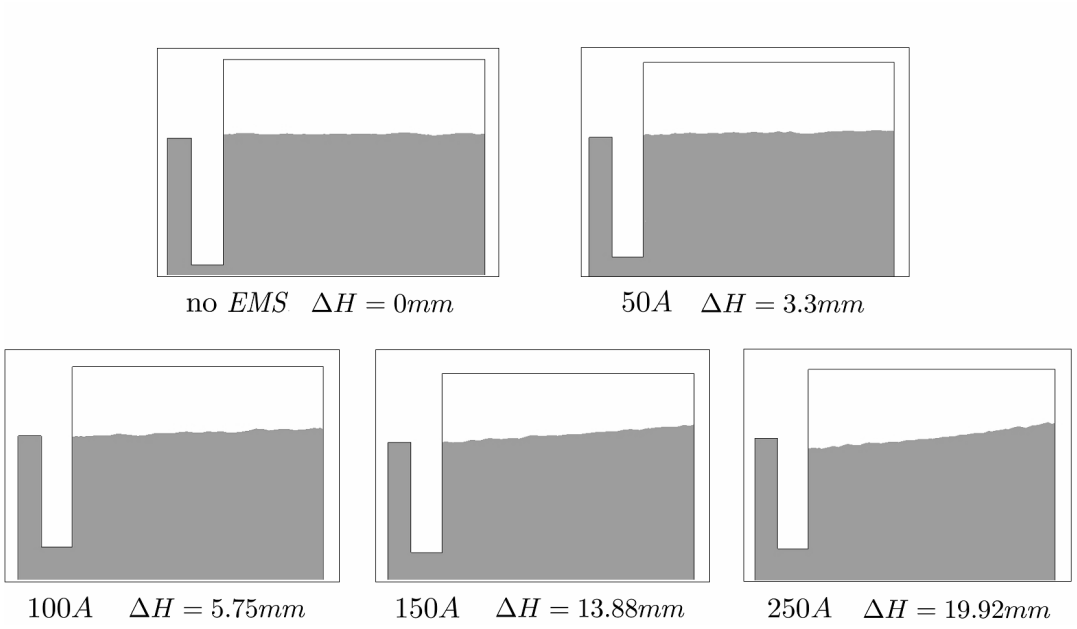

Figure 13. Electromagnetic Stirring in round billets mold. Deflection of the interface surface in mold.

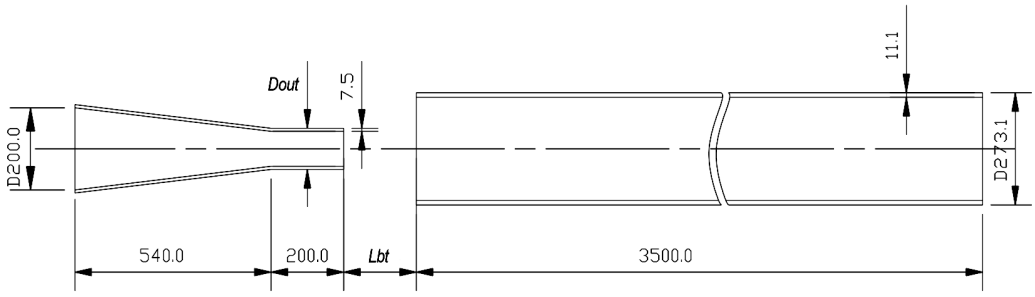

Figure 14. Heat treatment of steel tubes in water quenching pools. Scheme and dimensions of the nozzle-tube system.

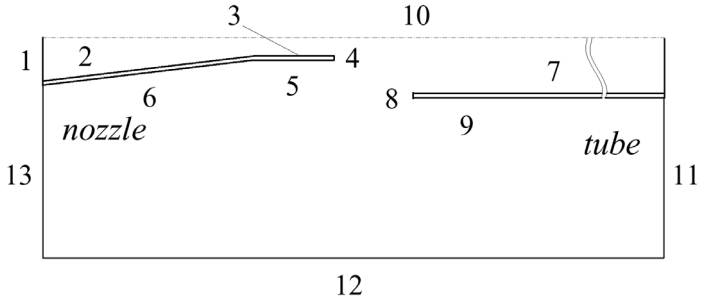

Boundaty Conditions:

1. Nozzle entrance: $v_r = 0$; $v_\theta = v_\theta{}^i$; $v_z = v_z{}^i$ $k = k^i$; $\varepsilon = \varepsilon^i$

2, 3, 5 and 6. Nozzle walls: $v_r = 0$; τ^w ; k^w ; ε^w .

4. Nozzle edge: $v_z = 0$; τ^w ; k^w ; ε^w .

7 and 9. Tube walls: $v_r = 0$; τ^w ; k^w ; ε^w .

8. Tube edge: $v_z = 0$; τ^w ; k^w ; ε^w .

10. Symmetry axis: $v_r = v_\theta = 0$; $\partial v_z / \partial r = 0$; $\partial k / \partial r = \partial \varepsilon / \partial r = 0$.

11. Domain limit: $\partial v_r / \partial z = \partial v_z / \partial z = \partial v_\theta / \partial z = 0$; $\partial k / \partial z = \partial \varepsilon / \partial z = 0$.

12. Domain limit: $v_r = 0$; $\partial v_z / \partial r = \partial v_\theta / \partial r = 0$; $\partial k / \partial r = \partial \varepsilon / \partial r = 0$.

13. Domain limit: $\partial v_r / \partial z = \partial v_\theta / \partial z = 0$; $v_z = 0$; $\partial k / \partial z = \partial \varepsilon / \partial z = 0$.

Figure 15. Boundary conditions for quenching pool model. v_z^i is determined from flow rate and v_θ^i from swirl number. Turbulent variables at inlet were imposed using Eq. 11 with α=0.01 and L=100 mm.

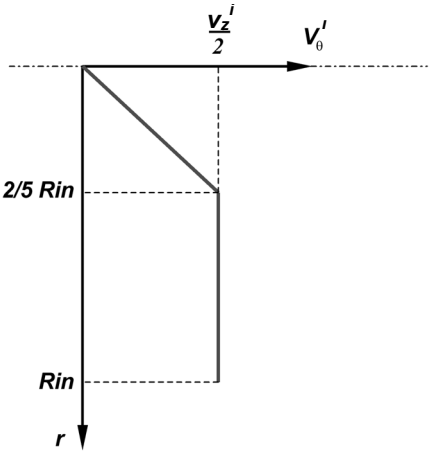

Figure 16. Heat treatment of steel tubes in water quenching pools. Azimuthal velocity profile used as boundary condition.

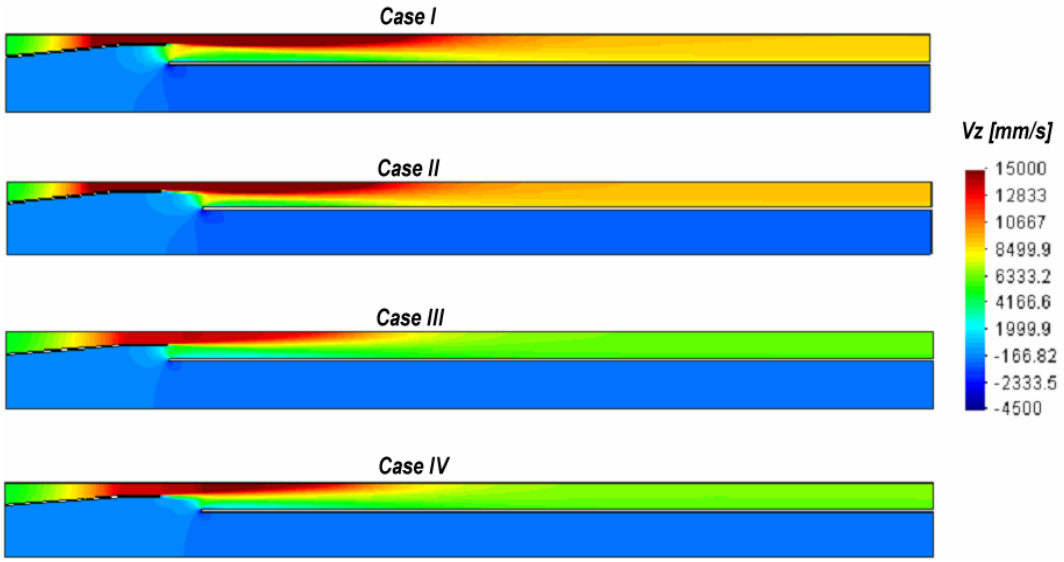

Figure 17. Heat treatment of steel tubes in water quenching pools. Axial velocity field for Cases I-IV.

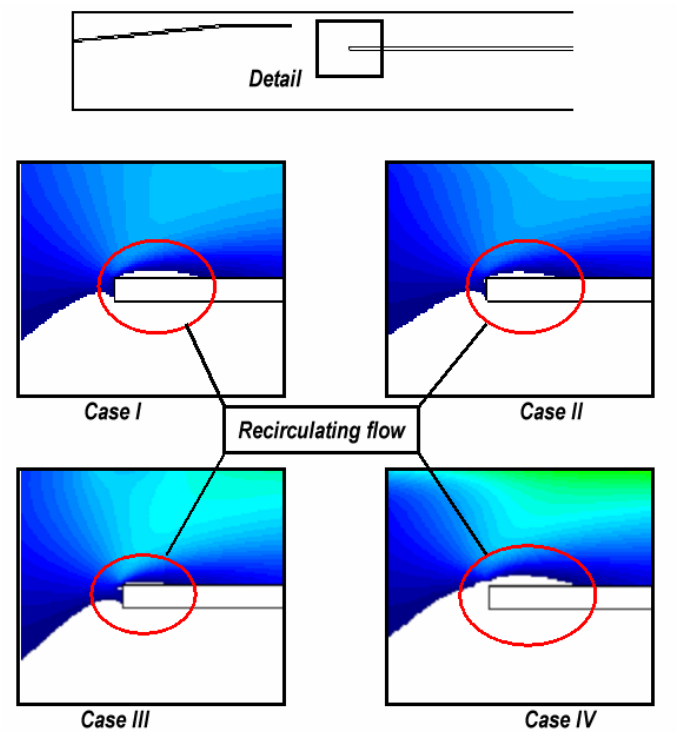

Figure 18. Heat treatment of steel tubes in water quenching pools. Recirculating flow on the inner tube wall. Cases I-IV.

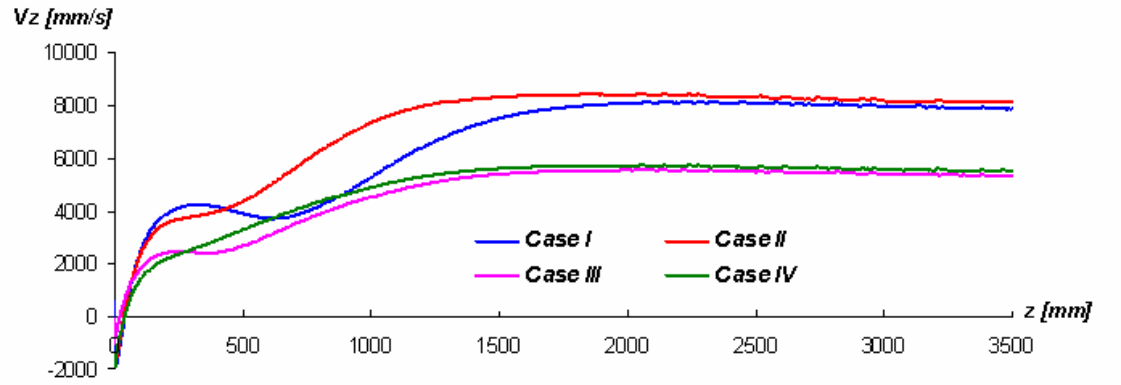

Figure 19. Heat treatment of steel tubes in water quenching pools. Axial velocity along the inner tube wall.

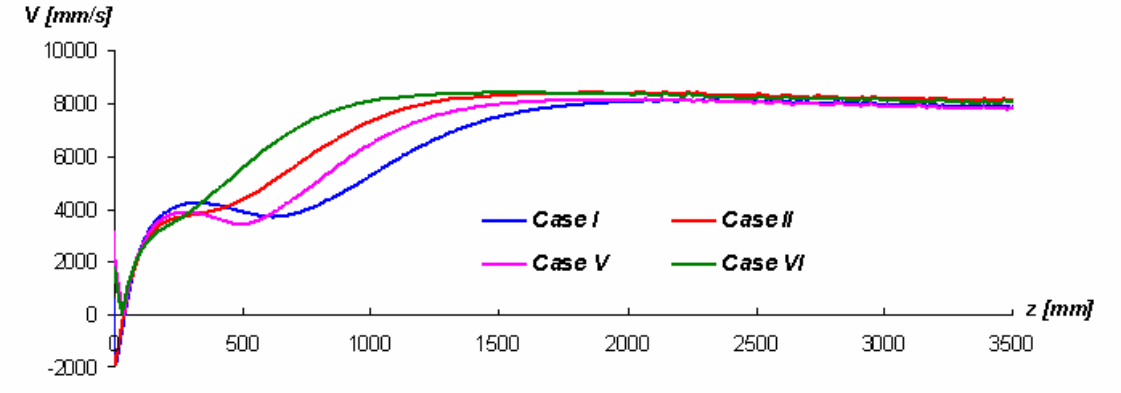

Figure 20. Heat treatment of steel tubes in water quenching pools. Velocity modulus along the inner tube wall. Cases I, II, V and VI.